PHYSICAL REVIEW B **74**, 054103 (2006)

Unidirectional magnetic-field gradients and geometric-phase errors during Fourier encoding using orthogonal ac fields

Louis-S. Bouchard

Materials Sciences Division, Lawrence Berkeley National Laboratory and Department of Chemistry, University of California Berkeley,
1 Cyclotron Road Building 11-D64, Berkeley, California 94720, USA

(Received 30 December 2005; revised manuscript received 23 May 2006; published 4 August 2006)

Nuclear magnetic resonance and imaging in very low fields is fundamentally limited by untruncated concomitant gradients, which cause severe distortions in image acquisition and volume selection if the gradient fields are strong compared to the static field. In this paper, it is shown that gradient fields oscillating in quadrature can be used for spatial encoding in low fields and provide substantial improvements over conventional encoding methods using static gradients. In particular, cases where the maximum applied gradient field ΔB_{max} is comparable to or higher than the static field B_0 over the field of view, i.e., $\Delta B_{max}/B_0 > 1$, are examined. With these gradients, undistorted volume selection and image encoding is possible because smaller geometric phase errors are introduced during cyclic motion of the Hamiltonian. In the low field limit, slice selection is achieved with a combination of soft pulse segments and a coherent train of hard pulses to average out concomitant fields over the fast scale of the Hamiltonian.

DOI: 10.1103/PhysRevB.74.054103 PACS number(s): 03.50.De, 07.55.Db, 76.60.Pc

I. INTRODUCTION

Pulsed-field gradient nuclear magnetic resonance (NMR) and magnetic resonance imaging (MRI) tomography[1,2] rely on Fourier encoding, a method by which the phase of the transverse magnetization is modulated by the application of a gradient in the component of the static field along some direction. To reconstruct the morphology of an object, multiple encodings are collected, and inverse Fourier transformation of the data set provides a map of the local spin density. At high fields, this description is accurate because the spin Hamiltonian, which also contains perpendicular "concomitant" components, is truncated by the strong Zeeman interaction. Truncation of the Hamiltonian is the averaging of rapidly oscillating concomitant components of the gradient field and is formally equivalent to first-order perturbation theory. Thus, a pure gradient can never be created by Maxwell's equations, however, truncation makes unidirectional gradients possible in the rotating frame.

At low fields, this picture no longer provides an accurate description of the spin dynamics. As the ratio $\Delta B_{max}/B_0$ is increased, the concomitant fields cause severe distortions in the phase encoding and slice selection. (ΔB_{max} is the maximum gradient field over the measurement region or field of view.) When $\Delta B_{max}/B_0 \sim 1$, for example, planes of isofrequency are bent into spheres whose radius equals one half the field of view.[3]

Low-field NMR and imaging systems are of great interest not only in chemistry and biomedicine, but also in physical science applications because of the possibility of smaller and portable devices with lower production and operational costs. Operation at low fields places smaller requirements on field homogeneity and the lower electromagnetic frequencies penetrate easily through metal objects,[4] while reducing dramatically the role of magnetic susceptibility artifacts. Increased T_1 contrast for imaging has been reported.[5] Also attractive is the possibility for measuring scalar couplings in microtesla fields[6] and the simultaneous detection of multiple nuclei with a single detector.

A portable low-field NMR device, the NMR MOUSE, has been developed by Blümich *et al.*[7] for materials and biomedicine. Applications to the characterization of products from technical elastomers, skin, and coatings on iron sheets have been demonstrated.[8] More recently, an 8 kg mobile scanner was developed using a Halbach magnet for measurements of porosity and pore-size distributions of water-saturated geological drilled cores.[9] Such portable devices are likely to be used in medical or paramedical applications in the near future, or deployed on the field for geological surveys, in research vessels or logging platforms,[10] and for surface measurements such as skin.[11] Imaging in the earth's magnetic field was demonstrated by Stepisnik.[12] Recent advances include imaging in microtesla fields using SQUID detection[5] and spectroscopy in a one-sided system.[13]

The move to lower fields is associated with a loss in sensitivity due to the lower thermal polarization. These problems can be overcome with the use of hyperpolarized gas[14–17] and parahydrogen-induced polarization. Time-of-flight remote NMR[18] measurements in microfluidic devices offer the possibility of noninvasive time-resolved imaging for monitoring reaction kinetics on a chip[19] with increased sensitivity. Despite the broad interest in low-field NMR for those many different areas of physics, problems still remain having to do with the presence of concomitant gradients and matching of the gradient tensor field to arbitrary desired excitations of the spin system.

A recent approach by Meriles *et al.*[20] uses a rapid train of dc magnetic-field pulses to eliminate the overall phase accumulated due to components of the concomitant field that are perpendicular to the axis of the pulses. The pulse train provides spatial encoding along the direction of the pulse axis. We have recently implemented the Meriles approach in μT fields using superconducting quantum interference device (SQUID) detection. Until now, SQUID imaging in low fields has only been possible with very moderate field gradient pulses, establishing a lower limit to the minimum time of an encoding sequence. This is an extremely important experimental drawback whenever experiments are done in a nonideal environment, and severely limits the possibility of fast measurements.

The Meriles method only applies at or near zero fields and is expected to break down at higher fields ($\gtrsim$mT) where the dynamics are described by a rotating frame. This article demonstrates that pairs of magnetic field gradients oscillating in quadrature produce significantly improved performance for spatial encoding and slice selection in low fields. In a regime where conventional MRI approaches are either useless or at best, perform poorly, the rotating gradient method takes advantage of stationary gradient-field components in the rotating frame to provide undistorted phase encoding. The remaining oscillatory components are linearly polarized rather than circularly polarized and much less effective in perturbing the intended trajectory. Slice selection is performed with a combination of hard and soft pulses and rotating-frame gradient fields with a coherent train of hard pulses designed to eliminate the problematic concomitant field component.

II. UNIDIRECTIONAL MAGNETIC-FIELD GRADIENTS

Unidirectional magnetic-field gradients are forbidden by the curl-free and divergence-free conditions on the magnetic field in a region with no currents. However, the electromagnetic forces acting on charged or neutral particles can be tailored for deflecting or trapping purposes using ac fields by exploiting the time average of those fields.[21,22] The principles of electromagnetic traps are reviewed in an article by Wolfgang Paul.[21] In this article, we examine the spin precession in a time-averaged magnetic-field gradient as it applies to the NMR problem of phase encoding.

A. Averaging Principle

The averaging principle for quantum spin systems of Haeberlen and Waugh,[23] also known as Average Hamiltonian Theory, is widely used in the analysis of NMR experiments. The zeroth-order contribution to the Magnus expansion is given by the time average of the Hamiltonian. Over small time intervals, this zeroth-order description can often be used to describe the evolution for complicated time dependences in the Hamiltonian.

For example, consider a Hamiltonian $H(\tau_f,\tau_s)$ characterized by two widely different time scales: τ_f and τ_s. τ_f is the fast scale and τ_s is the slow scale. Under certain conditions, the time average over the fast scale is sufficient to describe the dynamics of the spin system. Thus, for a Hamiltonian

$$H(t) = -\gamma[B_x(t)I_x + B_y(t)I_y + B_z(t)I_z] \tag{1}$$

describing the coupling of a spin $\mathbf{I}$ to a magnetic field $\mathbf{B}$, the dynamics in the limit of rapid oscillations are determined by the time average

$$H(\tau_s) = -\gamma[\overline{B_x}(\tau_s)I_x + \overline{B_y}(\tau_s)I_y + \overline{B_z}(\tau_s)I_z], \tag{2}$$

where the bar indicates a time average over τ_f. Time-averaged magnetic fields can be used to tailor the spatial dependence of spin precession. In the general case, and for descriptions over longer time intervals, higher-order terms in the Magnus expansion are used for a full description.[23,24]

B. Interaction Representation

Consider a Hamiltonian $H=-\gamma\mathbf{I}\cdot\mathbf{B}$ for the interaction of a spin $\mathbf{I}$ in a time-dependent magnetic field $\mathbf{B}$, which consists of a constant static component $B(\tilde{\mathbf{r}})\hat{\mathbf{z}}$, an applied gradient $(\mathbf{r}-\tilde{\mathbf{r}})\cdot\nabla\mathbf{B}(\tilde{\mathbf{r}})$ and an ac field $\mathbf{B}_1$. Using the summation convention on i and j indices, the Hamiltonian is

$$H(\mathbf{I};\mathbf{B})(\mathbf{r}) = -\gamma B(\tilde{\mathbf{r}})I_z - \gamma I_i(r_j-\tilde{r}_j)\partial_j B_i(\tilde{\mathbf{r}}) - \gamma \mathbf{I}\cdot\mathbf{B}_1, \tag{3}$$

where $\mathbf{r}=(x,y,z)$ and $\tilde{\mathbf{r}}$ is the origin. In what follows, we include γ into the scaling of B so the units of the gradient tensor $\partial_j B_i(\tilde{\mathbf{r}})$ are reported in rad/s/cm and the units of B are in rad/s. We abbreviate $\omega_0=-B(\tilde{\mathbf{r}})$, $\omega_1=-B_1$ and write H_G and H_{RF} for the parts of the Hamiltonian pertaining to the gradient and rf pulse, respectively.

Effecting a transformation to the interaction representation of the Zeeman interaction, $e^{i\omega_0 I_z t}(\cdot)e^{-i\omega_0 I_z t}$, transforms the Hamiltonian to

$$H' = e^{i\omega_0 I_z t}[-I_i(r_j-\tilde{r}_j)\partial_j B_i(\tilde{\mathbf{r}}) - \mathbf{I}\cdot\mathbf{B}_1]e^{-i\omega_0 I_z t}. \tag{4}$$

The terms containing I_z are invariant to this rotation transformation while I_x and I_y become time dependent. The components of the applied gradient field in I_x and I_y are called concomitant gradients in the NMR literature. In the limit of high fields, i.e.,

$$|\omega_0| \gg |(r_j-\tilde{r}_j)\partial_j B_i(\tilde{\mathbf{r}})|, \tag{5}$$

they oscillate rapidly and average to zero. This phenomenon is called truncation. Only the terms in I_z affect the spin dynamics at high fields. In low fields, the components in I_x and I_y perturb the motion significantly and must be accounted for. In particular, they may cause geometric phase errors to be discussed later.

For related reasons, we shall discuss only the case of circularly polarized ac fields

$$\mathbf{B}_1(t) = B_1[\cos(\omega_0 t+\varphi)\hat{\mathbf{x}} + \sin(\omega_0 t+\varphi)\hat{\mathbf{y}}], \tag{6}$$

which give rise to a stationary component in the rotating frame about which rotations of the spins can be performed. Linearly polarized ac fields $\mathbf{B}_1(t)=B_1\cos(\omega_0 t)\hat{\mathbf{x}}$ give rise to an undesirable time-dependent component which perturbs this motion.

C. Magnetic Resonance Imaging

In MRI experiments, equilibrium nuclear magnetization proportional to the total longitudinal spin angular momentum operator $I_z=\Sigma_{i=1}^N I_{z,i}$ is rotated into a transverse component, say I_x, and phase encoded using magnetic-field gradients of the form $I_z(\mathbf{g}\cdot\mathbf{r})$, where $\mathbf{g}$ is the gradient vector with components $g_i=\partial_i B_z$. This is because in high fields, static gradient components $\partial_i B_x$ and $\partial_i B_y$ are truncated in the interaction representation, unless ac gradients are used. The quadrature NMR signal measured is proportional to the volume integral of the weighted trace

$$F_+(t) = \int d^3\mathbf{r}\ \mathrm{Tr}[I_+ e^{iI_z \int_0^t \mathbf{g}(\tau)\cdot\mathbf{r}d\tau} I_x \rho(\mathbf{r}) e^{-iI_z \int_0^t \mathbf{g}(\tau)\cdot\mathbf{r}d\tau}]$$
$$\propto \int d^3\mathbf{r}\ \rho(\mathbf{r}) e^{i\mathbf{k}\cdot\mathbf{r}}, \qquad (7)$$

where $\mathbf{k}(t)=\int_0^t \mathbf{g}(\tau)d\tau$ is a wave vector which can be varied using a gradient wave form $\mathbf{g}(\tau)$. The weighting factor $\rho(\mathbf{r})$, also loosely referred to as the "local spin density," is proportional to the total spin angular momentum operator $\Sigma_i I_{z,i}$ contained in a volume element $d^3\mathbf{r}$ and is widely displayed as grayscale intensity in MRI images. [$\rho(\mathbf{r})$ also possibly reflects relaxation time weighting and/or specifics of the imaging pulse sequence in more complicated experiments; see Haacke[25] for details.] Inverse Fourier transformation gives the spin density $\rho(\mathbf{r})$. This principle of Fourier encoding is the basis of MRI.

In low fields, the time-evolution operator is no longer a rotation about I_z of the form $e^{i\mathbf{k}\cdot\mathbf{r}I_z}$ but corresponds to a rotation about a mixture of axes I_x, I_y, and I_z due to the presence of oscillating components in I_x and I_y. These concomitant components impart a significant phase error to the spins. The phase error is geometric in nature because it corresponds mainly to a tilting of the rotation axis. In the next section, we explore gradient schemes which avoid this problem.

It is customary to denote the maximum gradient field over the field of view (FOV) or sample volume, i.e., the quantity $\max_{\mathbf{r}\in FOV}\|(\mathbf{r}-\tilde{\mathbf{r}})\cdot\nabla\mathbf{B}\|$ by ΔB_{max}. We also follow the convention of writing $B_0=B(\tilde{\mathbf{r}})$ and fix the origin $\tilde{\mathbf{r}}=0$ at the center of the FOV. Significant distortions in the Fourier encoding arise when the ratio $\Delta B_{max}/B_0$ is comparable to or greater than one.

D. Rotating Frame Gradient Of The First Kind

In conventional MRI, magnetic-field gradients are typically generated by driving currents in electromagnetic coils designed to create a gradient in the z component of the static field.[26] The pulses are dc currents, i.e., the carrier frequency is zero. The contributions to the x and y components of the static field are ignored because of truncation. Consider instead two gradient coils, each driven by an ac current at the NMR resonance (Larmor) frequency, but the current in the first coil is 90° out of phase with the current in the second coil. The total gradient field therefore "rotates" at the Larmor frequency and can be used to generate stationary components for use in Fourier encoding, as we describe in this paper. We discuss two different configurations.

A gradient of the form

$$a(z\hat{\mathbf{x}} + x\hat{\mathbf{z}}) \qquad (8)$$

is added to another gradient field rotated by 90° about the z axis, with respect to the first one,

$$b(z\hat{\mathbf{y}} + y\hat{\mathbf{z}}), \qquad (9)$$

but with the second field driven by a current that is 90° out of phase with respect to the first field, i.e.,

$$a(t) = g\cos(\omega t + \varphi), \quad b(t) = g\sin(\omega t + \varphi). \qquad (10)$$

Thus, the two gradient coils are geometrically orthogonal to each other, whereas their currents are phase-orthogonal. The contribution of this gradient field to the interaction representation Hamiltonian is

$$H_G^{(\mathrm{I})\prime}(\mathbf{r}) = zg\cos\varphi I_x + zg\sin\varphi I_y$$
$$+ g[x\cos(\omega t + \varphi) + y\sin(\omega t + \varphi)]I_z. \qquad (11)$$

We note that the rotating-frame transformation of the interaction representation refers to the rotation of spin space angular-momentum operators I_x, I_y, and I_z rather than laboratory frame coordinates (x, y, and z). Taking $\varphi=0°$ gives a time independent z gradient field in I_x, while $\varphi=90°$ gives a time-independent z gradient field in I_y. The time dependence of the gradient has been relinquished to an oscillating field along I_z. It turns out that this type of Hamiltonian with linearly polarized oscillating components possesses better averaging properties than one with rotating components. I will show that it performs better Fourier encoding and volume selection along z in low fields.

E. Rotating Frame Gradient Of The Second Kind

The second configuration utilizes a linear superposition of a field

$$a(y\hat{\mathbf{x}} + x\hat{\mathbf{y}}) \qquad (12)$$

with another field

$$b(-x\hat{\mathbf{x}} - y\hat{\mathbf{y}} + 2z\hat{\mathbf{z}}) \qquad (13)$$

scaled by ϵ. If these two fields are operated 90° out of phase, their contribution to the interaction representation Hamiltonian is

$$H_G^{(\mathrm{II})\prime}(\mathbf{r}) = [-\epsilon xg\sin(\omega t + \varphi) + yg\cos(\omega t + \varphi)]$$
$$\times\left(\frac{I_+ e^{i\omega_0 t} + I_- e^{-i\omega_0 t}}{2}\right) + [xg\cos(\omega t + \varphi)$$
$$-\epsilon yg\sin(\omega t + \varphi)]\left(\frac{I_+ e^{i\omega_0 t} - I_- e^{-i\omega_0 t}}{2i}\right)$$
$$+ I_z[\epsilon 2zg\sin(\omega t + \varphi)]. \qquad (14)$$

In the special case $\epsilon=1.0$, this field has the following features. The x gradient Hamiltonian in the rotating frame is time-independent in I_x for $\varphi=90°$ or in I_y for $\varphi=0°$. The y gradient rotates at a rate 2ω, while the z gradient oscillates in I_z at rate ω. Likewise, stationary y gradients in the rotating frame can be obtained by taking

$$a(-y\hat{\mathbf{x}} - x\hat{\mathbf{y}}) \qquad (15)$$

instead of

$$a(y\hat{\mathbf{x}} + x\hat{\mathbf{y}}), \qquad (16)$$

or equivalently, by inverting the sign of ϵ.

F. Geometric Phase Of Encoding Gradient

We now look at the averaging properties of rotating-frame gradients versus conventional gradients. Their performance

TABLE I. The parameter $f=100\%\times[(\phi_{tot}-\phi_{dyn})/\phi_{dyn}]$ gives the percentage geometric phase relative to the dynamical phase. The solid angle of the motion is $\Omega(\alpha)=\int d\Omega=\int_0^{2\pi}\int_1^{\cos\alpha}d(\cos\theta)d\phi$.

Trajectory	α (rad)	B_1 (rad/s)	ϕ_{tot} (rad)	ϕ_{dyn} (rad)	f (%)	$\phi_{tot}-\phi_{dyn}$ (rad)	$\Omega(\alpha)$ (sr.)
$\mathbf{B}_A$	0.1	10.0	9.89	9.87	0.2	0.02	0
	0.1	20.0	19.75	19.75	0.02	0.005	0
	0.2	10.0	9.98	9.87	1.1	0.11	0
	0.2	20.0	19.77	19.75	0.1	0.02	0
$\mathbf{B}_C$	0.1	10.0	10.03	9.87	1.6	0.16	0.0314
	0.1	20.0	19.78	19.77	0.05	0.01	0.0314
	0.2	10.0	10.56	9.87	7.0	0.69	0.1252
	0.2	20.0	19.86	19.75	0.6	0.11	0.1252

can be quantified by a phase error, which corresponds to the difference between the intended phase imparted by a stationary magnetic field gradient and the actual phase obtained in the presence of time-dependent concomitant components. For a magnetic moment $\mathcal{M}$ precessing about a magnetic field $\mathbf{B}$,

$$\frac{d\mathcal{M}}{dt}=\mathcal{M}\times\mathbf{B} \tag{17}$$

and it is possible to define a phase angle in the plane perpendicular to $\mathbf{B}$ if the motion of $\mathbf{B}$ is slow enough. This example of Berry's phase for a classical spin has been treated classically using Hannay's angle.[27–29]

Let $\mathbf{B}=B\mathbf{b}$ while (I,φ) are canonical action-angle variables on the sphere S^2 with $I=\mathcal{M}\cdot\mathbf{b}$ and φ is the angle in the $(\mathbf{e}_1,\mathbf{e}_2)$ plane that is perpendicular to the unit vector $\mathbf{b}$. The two-form

$$dI\wedge d\varphi=-S\sin\theta\, d\theta\wedge d\varphi \tag{18}$$

is proportional to the area element on S^2 and defines a symplectic form on S^2. The Hamiltonian in action-angle variables has the form $H(I;\mathbf{B})=BI$, where $\mathbf{B}$ plays the role of the external parameter. At the end of a slow cycle in $\mathbf{B}$, the magnetic moment $\mathcal{M}$ is back on its circle of precession at $t=1$ and its position is shifted by

$$\varphi(1)-\varphi(0)=\int_0^1 B(t)dt-\frac{\partial}{\partial I}\oint\langle pd_Bq\rangle, \tag{19}$$

where $p:=\mathcal{M}_z$ and $q:=\arctan[\mathcal{M}_y/\mathcal{M}_x]$. d_B denotes the exterior derivative in the parameter space of the Hamiltonian and

$$\langle pd_Bq\rangle=\frac{1}{2\pi}\int_0^{2\pi}p(\varphi,I;\mathbf{B})d_Bq(\varphi,I;\mathbf{B})d\varphi \tag{20}$$

is the torus average, which arises in the adiabatic limit. In this adiabatic limit, the geometric angle equals[30]

$$-\frac{\partial}{\partial I}\oint\langle pd_Bq\rangle=\Omega(C), \tag{21}$$

where $\Omega(C)$ is the solid angle subtended by the closed curve C on the parameter manifold $\mathbf{B}=\text{const}$. When the adiabaticity is relaxed, it is still be possible to define a geometric phase if the precession, which begins perpendicular to the effective field, remains mostly perpendicular to it during the motion, however, the geometric phase deviates from the above solid angle formula.

Consider the following two closed curves where t varies from 0 to 1 s. The arc trajectory,

$$\mathbf{B}_A(t)=\hat{\mathbf{y}}B_1\sin\alpha\sin(2\pi t)+\hat{\mathbf{z}}B_1\sqrt{1-[\sin\alpha\sin(2\pi t)]^2}, \tag{22}$$

begins parallel to $\hat{\mathbf{z}}$ $(t=0)$, then tilts by an angle α toward $-\hat{\mathbf{y}}$, then toward $+\hat{\mathbf{y}}$ and back to $\hat{\mathbf{z}}$ $(t=1)$. The maximum angular rate of rotation for $\mathbf{B}_A$ about the $\hat{\mathbf{x}}$ axis is $\sin(\alpha)2\pi$ rad/s, which gives 0.63 rad/s for $\alpha=0.1$ rad and 1.25 rad/s for $\alpha=0.2$ rad.

The circular trajectory

$$\mathbf{B}_C(t)=\hat{\mathbf{x}}B_1\sin\alpha\cos(2\pi t)+\hat{\mathbf{y}}B_1\sin\alpha\sin(2\pi t)+\hat{\mathbf{z}}B_1\cos\alpha, \tag{23}$$

where α is the spherical polar angle measured from the $\hat{\mathbf{z}}$ axis. The motion of $\mathbf{B}_C$ is circular about the $\hat{\mathbf{z}}$ axis with angular velocity 2π rad/s.

The above rates of change (2π, 0.63, and 1.25 rad/s) are to be compared with the rate of precession of the magnetization vector about the effective field $B_1=10$ rad/s and 20 rad/s. Except for the case 2π rad/s, these cyclic trajectories are adiabatic.

Table I shows numerical calculations of the geometric phase obtained by evolving the initial condition $\mathcal{M}=\hat{\mathbf{x}}$ over one period where t ranges from 0 to 1. During the trajectory, the total phase $\phi_{tot}=\varphi(1)-\varphi(0)$ is calculated as the total angle traced by the magnetization vector $\mathcal{M}(t)$, including all windings, as the magnetization nutates about the $\hat{\mathbf{z}}$ axis while mostly remaining near the xy plane. A conventional gradient behaves like the $\mathbf{B}_C(t)$ trajectory whereas the quadrature rotating-frame gradient behaves as $\mathbf{B}_A(t)$. In the case of

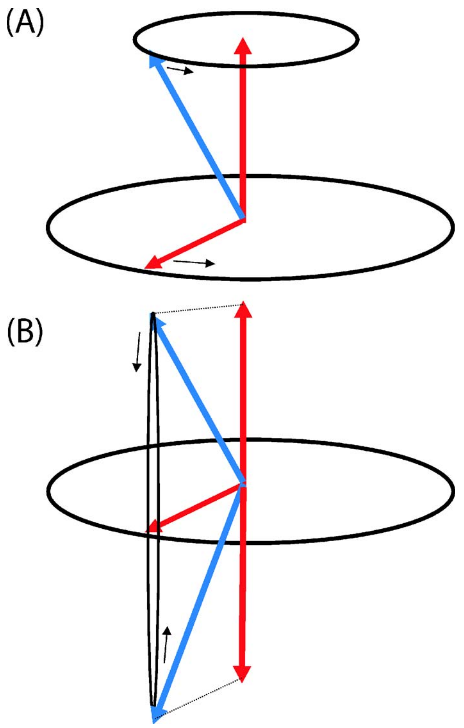

FIG. 1. (Color online) Hamiltonian motions in the interaction representation during one rotating frame oscillation for: (A) conventional static imaging gradient with rotating concomitant fields and (B) type I rotating frame gradient with linearly polarized concomitant component.

quadrature rotating-frame gradients the relative phase errors, as quantified by the f parameter, are considerably lower.

Figure 1 shows a comparison of the Hamiltonian cycles for the case of conventional imaging gradient versus rotating-frame gradient (type I). The most obvious difference is the respective solid angles during the motion.

III. FOURIER ENCODING

To compare the method to conventional phase encoding, we numerically calculate the magnetization evolution under time-independent gradients and quadrature rotating-frame gradients. Rotations induced by rotating-frame gradients take place about the I_y axis. Therefore, the magnetization is nutated primarily in the xz plane. For conventional MRI gradients, magnetization is modulated about I_z, so that nutations would be expected to take place in the xy plane. Deviations to this expected behavior are due to nonsecular gradient components.

Calculations were performed on a Pentium IV machine using FORTRAN 90 code compiled using version 8.1 of the Intel Fortran compiler for Linux. The density operator is propagated from initial to final states, using at least 100 subdivisions of the time axis per oscillation period of the rotating frame to calculate the time-ordered product of matrix exponentials[31] $U(T_c)=\Pi_{i=1}^{100}\exp(-iH_i dt)$ to approximate the propagator, where H_i is a step-function approximation to $H'(t)$. The only calculations involved are time evolutions under the rotating-frame gradient Hamiltonian for a given amount of time.

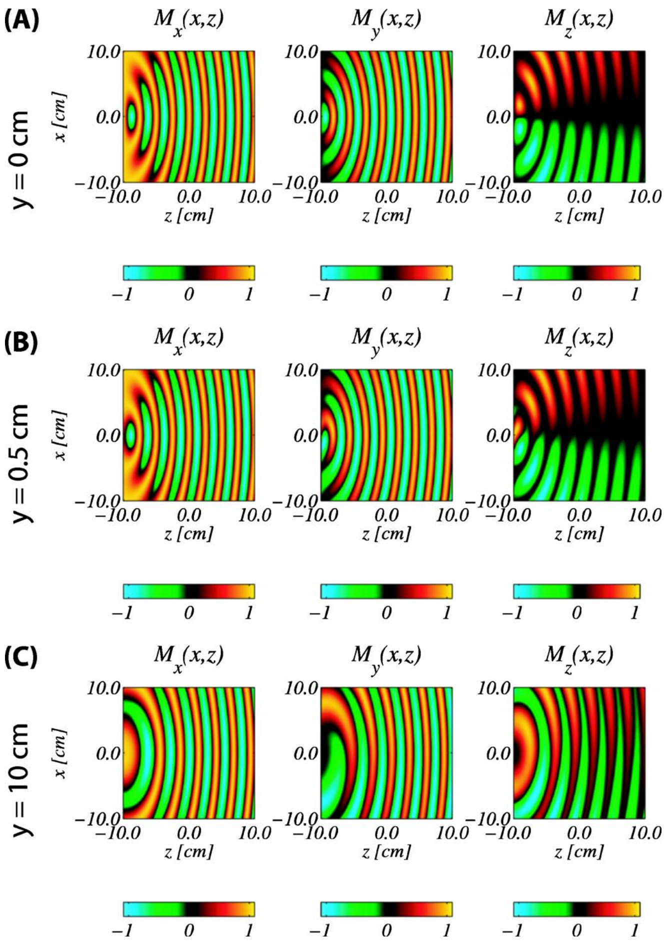

FIG. 2. (Color online) Conventional Fourier encoding along z with Maxwell coil in the presence of concomitant gradients operated at constant current and $\Delta B_{max}/B_0 \sim 1.0$. Curved surfaces rather than planes of constant phase are produced. Magnetization along xz for planes at (A) $y=0$ cm, (B) $y=0.5$ cm, and (C) $y=10$ cm. Encoding produced by applying a 62 872 rad/s/cm gradient in a 628 716 rad/s static field for 40 μs.

A. Conventional Imaging Gradients

Figure 2 illustrates the effects of concomitant gradient fields on Fourier encoding for a Maxwell coil with field $g(x\hat{\mathbf{x}}+y\hat{\mathbf{y}}-2z\hat{\mathbf{z}})$ and $\Delta B_{max}/B_0 \sim 1.0$. The intent is to produce a modulation along z. Instead of a linear phase dependence along z, the modulation depends on x because of deviations caused by the nonsecular concomitant fields. Here, $\Delta B_{max} = gFOV/2$, where $FOV=20$ cm is the field of view. The distortions in the spatial encoding also depend on y, as can be seen by comparing Fig. 2(A) to Figs. 2(B) and 2(C), which are plots of the magnetization following a constant gradient pulse applied for 40 μs. The corresponding results for the magnetization plots in yz planes identical to the xz planes are due to the symmetry of this gradient. This renders the conventional gradient useless when the ratio $\Delta B_{max}/B_0$ is large.

Figure 3 shows similar plots of magnetization following a constant gradient pulse ($\Delta B_{max}/B_0 \sim 1.0$), for a Golay pair as

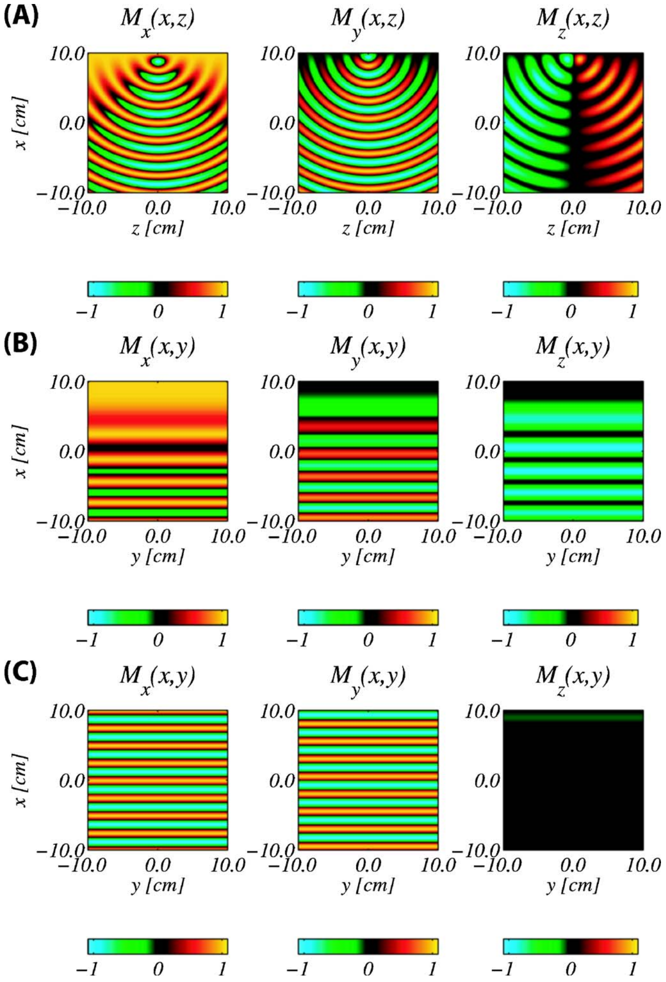

FIG. 3. (Color online) Conventional Fourier encoding along x with a saddle coil operated with constant current such that $\Delta B_{max}/B_0 \sim 1.0$. Magnetization is plotted (A) in the xz plane at $y=0$ cm, in the xy plane at $z=10$ cm (B), and at $z=0$ cm (C). Encoding produced by applying a 62 872 rad/s/cm gradient in a 628 716 rad/s static field for 40 μs.

used in conventional MRI. Such coils are normally used to provide modulations along x and y. The total field is $g(z\hat{\mathbf{x}}+x\hat{\mathbf{z}})$ and includes a concomitant component along z. This component is responsible for the heavy distortions in the modulation profile. Figure 3(A) shows the greatest distortions in the xz ($y=0$ cm) plane. The least distortion is seen in the plot of magnetization along xy, as shown in Fig. 3(C), for the plane $z=0$ cm. However, distortions increase with z, as seen in Fig. 3(B) for the case $z=10$ cm.

In both cases of Maxwell or Golay pair coils, a similar behavior is observed in which curved surfaces converging towards a common attractor whose location, according to Yablonskiy,[3] is a focal point for these concentric surfaces and the radius of curvature is $R_c=B_0/g$.

B. Rotating Frame Gradients

In Fig. 4 are plots of the magnetization profile in a 20 cm field of view following 40 μs of evolution in a quadrature rotating-frame gradient for which $\Delta B_{max}/B_0 \sim 1.0$. Figure 4(A) shows a z modulation produced using a type I rotating-frame gradient which is to be compared with the pattern of Fig. 2(A). The single focal point is split in two opposite attractor points, resulting in lower overall curvature of the phase profile. The smaller phase errors are due to the smaller solid angle traced by the Hamiltonian trajectory.

If a square region is cut out of this magnetization profile at 45° to the field of view (Fig. 4), the modulation is close to ideal, with displacements of the isofrequency sets along the direction of curvature less than 5% of the length of the corresponding isofrequency segment. The area of this reduced field of view is $1/\sqrt{2}$ the original field of view; this is equivalent to undistorted Fourier encoding with $\Delta B_{max}/B_0 \sim 0.7$.

To realize Fourier encoding of MRI slices in the xz and yz plane, this type of gradient presents a substantial improvement for imaging under conditions of strong gradient fields, i.e., when $\Delta B_{max}/B_0 \gtrsim 0.5$, over conventional static gradients. A simulated MRI image is shown in the next section which documents the improved spatial encoding.

Rotating frame type II gradients also provide improved spatial encoding in the case of magnetization modulations along x and y within an xz or yz slice, respectively. The results in Figs. 4(B) and 4(C) were produced with a scaling factor $\epsilon=0.5$. This choice of ϵ reduces the impact of the oscillating concomitant component along I_z, which is responsible for much of the distortion in the encoding. This comes at the price of a slight oscillatory perturbation in the static concomitant component of the gradient along I_y; however, results show that this error is tolerable. Again, this improved performance can be understood in terms of geometric phase, with the exception of a rotating 2ω term in the transverse plane. However, this component is small in the neighborhood of $y=0$.

As for the case of a conventional static gradient, the magnetization profile degrades further as the plane is moved away from the origin (data not shown). However, for the purposes of Fourier encoding a slice whose thickness is 1 cm, the profile is sufficiently constant across the slice thickness when $\Delta B_{max}/B_0 \sim 1.0$.

C. Image Acquisition

Distortions in the phase encoding ultimately translate into image distortions. In the limit $|\mathbf{k}| \rightarrow 0$, there are no significant distortions to the phase encoding simply because there is no evolution under the gradient fields. Distortions from concomitant gradients increase with spatial frequency. To illustrate image distortion effects, the phase encoding process is simulated in Fig. 5.

A 128×128 single shot echo-planar imaging (EPI) readout, i.e., where k space is acquired continuously in a raster fashion on a rectangular grid of size 128×128, is applied to the 128×128 proton density maps of Figs. 5(A) and 5(C). Conventional high-field MRI images [Figs. 5(B) and 5(D)] faithfully represent the respective proton density maps while acquisition in low field [Figs. 5(E) and 5(G)] suffers from heavy distortions, ghosting and blurring over most of the field of view ($\Delta B_{max}/B_0 \sim 3.2$ at 10 cm from the center).

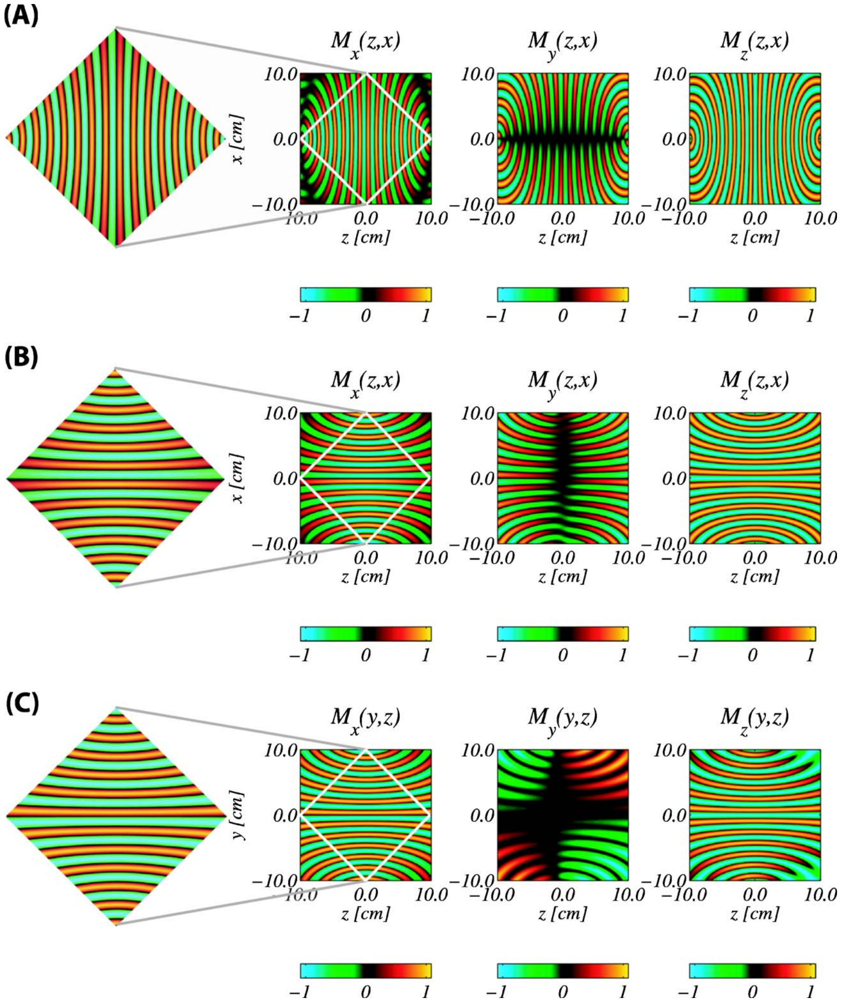

FIG. 4. (Color online) Magnetization profile obtained after 40 μs of evolution in a 62 872 rad/s/cm gradient and 628 716 rad/s static field ($\Delta B_{max}/B_0 \sim 1.0$) under (A) type I and (B,C) type II rotating frame gradients (with ϵ=0.5). In (B) x and (C) y modulations are shown. Subsets of the field of view where the modulation in M_x is most uniform are enlarged.

Most of these artifacts are absent over the middle $1/\sqrt{2}$ region of the field of view in the case of quadrature rotating-frame gradient encoding [Figs. 5(F) and 5(H)].

IV. VOLUME SELECTIVITY

The topic of volume selectivity is of central importance to modern MRI. It concerns the excitation of nuclear spins only within a desired volume. Conventional volume selection is done by applying pulses in the presence of static gradient fields. In the presence of concomitant gradients, conventional methods are easily rendered useless. We explain how the averaging principle can be used to combine conventional with hard pulses and rotating-frame gradients to avoid such distortions.

A soft pulse intermittently interrupted by a fast train of coherent hard pulses at regular intervals is described by a Hamiltonian with two time scales $(H_{RF}+H_G)'(\tau_s,\tau_f)$, where τ_s is the slow time scale of modulations in the soft pulse envelope and τ_f is the rapid scale of the hard pulse cycle. Averaging over one period removes the dependence on the fast scale, giving an effective Hamiltonian $\overline{(H_{RF}+H_G)}'(\tau_s)$. Consider the following two cases.

In the zero static field case, $H_G'=gzI_x+gxI_z$ and $H_{RF}'=\omega_1(t)I_y$. Therefore,

$$\overline{(H_{RF}+H_G)}' = \omega_1(t)I_y + gzI_x \qquad (24)$$

for a soft pulse $\omega_1(t)$, which contains the coherent pulse train of Eq. (A2) designed to remove I_z. In the low field case with a type I gradient, $H_G^{(I)\prime}$ is given by Eq. (11) with $\varphi=0°$, so that

$$\overline{(H_{RF}+H_G^{(I)})'} = zgI_x + \omega_1(t)I_y + \overline{g[x\cos(\omega t) + y\sin(\omega t)]}I_z. \qquad (25)$$

If $2\pi/\omega$ is large compared to the repetition period of the hard pulse train, the time-dependent term is nearly constant from the perspective of the coherent pulse train and the I_z term vanishes. In the other limit, the time-dependent terms oscillate rapidly and their effect is minimal. This is the case of truncation at high field.

Consider the following two schemes for slice selection, which assume an ac field polarized along I_x. The first scheme uses a type I rotating-frame gradient whose Hamiltonian, $H_G^{(I)\prime}$ [Eq. (11)], can be made to provide a z gradient along I_y. The second scheme uses a type II gradient [Eq. (14)] to produce a stationary x or y gradient along I_y in the rotating frame. We first rotate all I_z magnetization into I_y using a 90° pulse and then apply a soft (narrow-band) 90° pulse along I_x in the presence of a z gradient whose field is along I_y, i.e., a

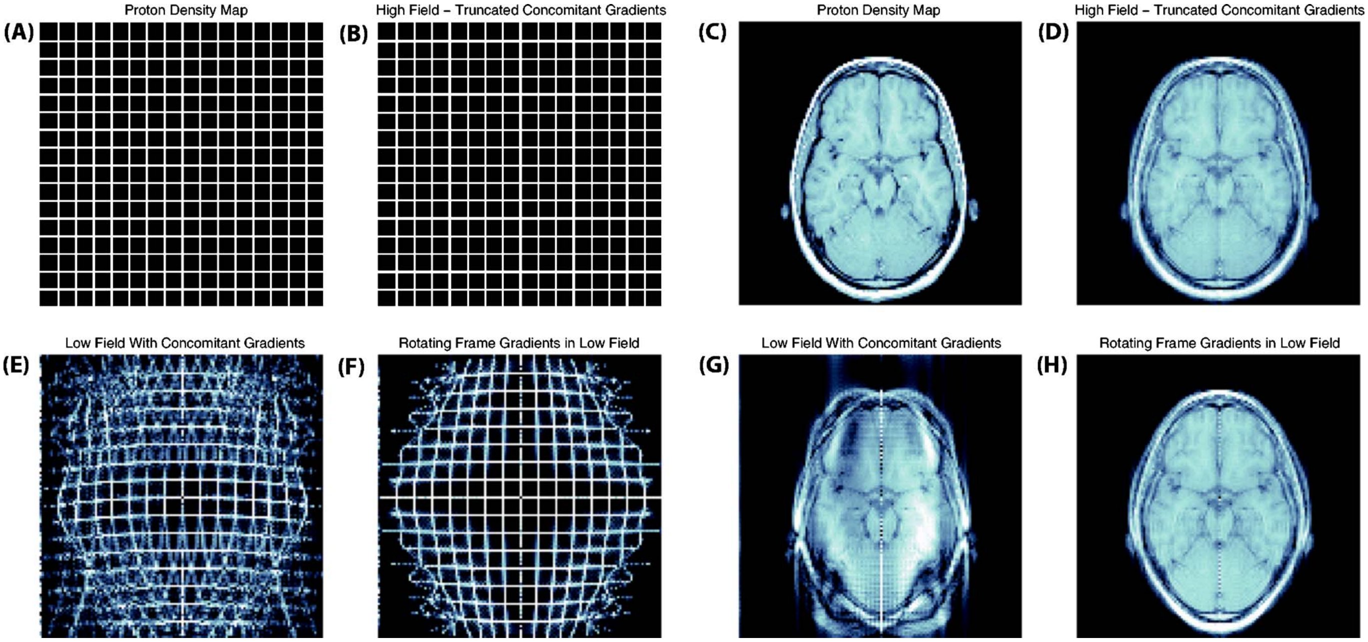

FIG. 5. (Color online) Single shot EPI using proton density maps (128×128) as input parameters (A,C) for a Cartesian grid phantom (A,B,E,F) and axial slice of human brain (C,D,G,H). The 20 cm field of view (yz plane) is phase encoded in 128×128 steps by simulating an echo-planar readout. (B,D) High-field images with conventional MRI encoding gradients ($\Delta B_{max}/B_0 < 0.1$). (E,G) Conventional low-field MRI images ($\Delta B_{max}/B_0 \sim 3.2$) with saddle pair and Maxwell coils. (F,H) Low-field images ($\Delta B_{max}/B_0 \sim 3.2$) with quadrature rotating-frame gradients. Gradient strength was 26 741 rad/s/cm. Field strength was 85 120 rad/s.

term $g_z z I_y$ in the Hamiltonian. The soft pulse rotates I_y towards $-I_z$ within its bandwidth, and leaves spins unaffected outside its bandwidth. With the excited spins along $-I_z$, spatial encoding is then performed with a rotating-frame gradient. The MRI signal is contained in the x and z components of the magnetization. A readout of the x component of magnetization provides the in-phase NMR signal while permitting further subsequent encoding of this magnetization. To get the quadrature component, a second acquisition with a $\pi/2$ phase shift in the excitation will do. We now explain how to generate the selective pulse.

Consider a soft pulse such as the Geen & Freeman[32] wave form. To produce a selective pulse which averages out the I_z term to zero during its course, we modify the soft pulse by inserting the following coherent train of hard pulses:

$$\{2\tau-(\pi_y)-\tau-(\pi_z)-2\tau-(\pi_{-z})-\tau-(\pi_{-y})-2\tau\}_n, \tag{26}$$

where τ and 2τ delays indicate intervals within which small segments of the soft pulse are applied. The soft pulse is interrupted at each hard pulse. The cycle is repeated until the entire soft pulse is executed. We found that τ should be roughly three orders of magnitude less than the total pulse duration for the averaging to be effective. The exact figure depends on the shape of the soft pulse with smoother shapes generally less demanding of the coherent train. The new pulse will be slightly longer. Its length increases by the total duration of the hard pulses added. This produces a pulse with two widely different time scales over which we may average out the fast scale.

For strong concomitant gradients ($\Delta B_{max}/B_0 \gtrsim 1.6$), conventional MRI slice selection schemes are incapable of producing slices without a severe amount of distortion, as seen in Figs. 6(A) and 6(D). The slice profile, which should be rectangular, is heavily distorted into a spherical shell with significant amounts of excitation occurring outside the intended slice. Figures 6(B) and 6(C) illustrate slice selection on axis ($y=0$ cm) along x or y using a type II rotating-frame gradient with $\epsilon=1.0$. While the performance is slightly degraded when going off axis ($|y|=10$ cm), as seen in Figs. 6(E) and 6(F), the degradation is far less important than the conventional case of Figs. 6(A) and 6(D), and such distortions are only significant near the edges ($|y|>8$ cm) of the volume.

The case of conventional slice selection with an applied z gradient from a Maxwell coil ($\Delta B_{max}/B_0 \sim 1.6$) is shown in Figs. 6(G) and 6(H). Although the performance is slightly better than a Golay pair generating an orthogonal slice on axis [compare Figs. 6(H) and 6(A)], the slice profile suffers from a heavy elliptical curvature and strong contamination originating from outside the intended volume. It is clear that conventional MRI gradient encoding performs poor slice selection in the regime $\Delta B_{max}/B_0 \sim 1.6$. In contrast, a type I rotating-frame gradient provides clean slice selection both on and off axis, as seen in Figs. 6(I) and 6(J). It was found that this type I gradient performs equally well in the asymptotic regime $\Delta B_{max}/B_0 \gtrsim 25$ (data not shown).

V. DISCUSSION

Rotating-frame gradients possess better properties for spatial encoding than conventional static gradients in the ultra-

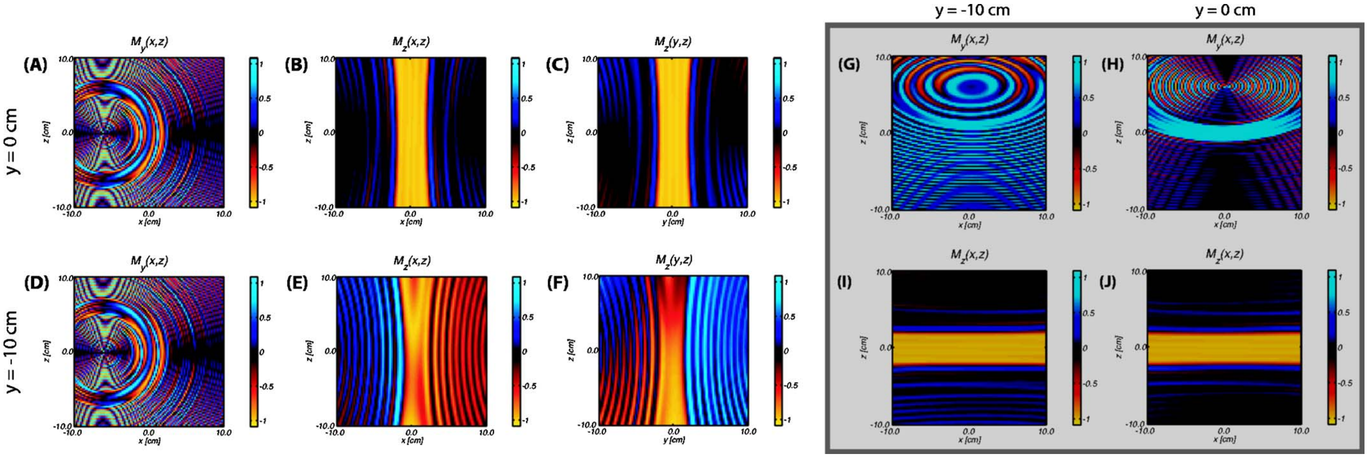

FIG. 6. (Color online) Comparison of static and type II rotating-frame gradients for slice-selection in the case $\Delta B_{max}/B_0 \sim 1.6$: Plots (A,D) are the slice-selection profiles for a saddle-pair gradient along x for xy planes at $y=0$ and -10 cm, respectively. (B,E) is the x slice selection using type II gradients with a stationary x gradient. (C,F) is the y slice selection for a type II gradient with stationary y gradient field. Parameters were $\tau = 15.75$ μs, subunit duration; 126 μs; pulse duration; 10 ms; 79 subunits per pulse, gradient; 1605 rad/s/cm, static field; 10 080 rad/s (1 cycle lasts 623 μs; there are 16 cycles across the pulse duration). Comparison of slice selection along z for a conventional Maxwell coil and a type I rotating frame gradient: Plots (G,H) are for the static Maxwell coil. (I,J) are for a type I gradient. xz planes are aligned according to: (G,I) 10 cm off center and (H,J) on axis. Parameters were $\tau = 15.75$ μs, subunit duration = 126 μs, pulse duration = 10 ms, 79 subunits per soft pulse, gradient = 1605 rad/s/cm, static field = 10 080 rad/s (1 cycle lasts 623 μs; there are 16 cycles across the pulse duration) so that $\Delta B_{max}/B_0 \sim 1.6$ and FOV=20 cm. Nearly identical performance is obtained at $\Delta B_{max}/B_0 \sim 25$.

low-field regime, where nonsecular terms in the Hamiltonian must be included in the analysis. Since the nutations of magnetization under the gradient primarily occur about an axis in the transverse plane, the gradients act as excitation pulses and the effects of magnetic-field inhomogeneities and susceptibility artifacts during gradient evolution are not of concern.

Quadrature ac excitation and rotating-frame gradient fields reduce the impact of nonsecular terms in the Hamiltonian. These improvements are most beneficial when Fourier encoding coronal or sagittal planes (xz or yz), as seen in Fig. 4, or when selecting a slice in a strong gradient (Fig. 6). The EPI images of Fig. 5 demonstrate that nearly undistorted image encoding is possible in regimes where the concomitant gradient fields are several times stronger than the Zeeman field.

While the time dilation factor in the average Hamiltonian $H^{(0)\prime} = \frac{1}{2}(aI_x + cI_z)$ characterizing the coherent part of the selective pulse (see Appendix) is equivalent to scaling down the gradient amplitudes by a factor of 2, the results of Fig. 6 show that slice selection can be done in conditions where $\Delta B_{max}/B_0 \gtrsim 25$. This regime is well beyond the scope of applicability of conventional slice selection pulse and gradient methods. Immunity to distortions (Fig. 6) can be achieved under conditions where the gradient field is an order of magnitude larger than the static field. Applications are not limited to imaging, but include undistorted pulsed-field gradient diffusion measurements and coherence pathway selection in low fields.

Radio frequency gradients have been successfully implemented for NMR spectroscopy and imaging by several investigators,[33–35] however, their advantageous properties for low-field imaging when used in quadrature appear to have been overlooked. The gradient fields discussed herein can be generated using tuned and matched circuits.[33] Rapid point readouts interleaved with oscillating gradient pulses have been implemented by Raulet *et al.*[33] and may require active feedback[36] or Cartesian feedback[37] approaches to rapidly suppress coil ringing. While rf power deposition from oscillating gradients and rf pulses is an important concern at high fields because of the strong electric fields and associated sample heating, this is not an issue at low fields, where contributions from the electric field are negligible and energy absorption is orders of magnitude lower.

A. Further Challenges

A number of important issues in low-field NMR still remain. Intrinsically low thermal polarization states may require the use of hyperpolarized agents or prepolarization with a stronger field. Detection of weak signals requires more sensitive detection methods such as SQUID or laser magnetometer. With portable NMR devices, the static magnetic field $\mathbf{B}(\mathbf{r})$, which varies both in strength and direction over space, is more conveniently described by a tensor field $\partial_j B_i(\mathbf{r})$ upon which a general spin excitation scheme attempts to match the evolution in a spatially varying gradient affecting any component of the local field. A recent approach to tackle variations in the static field amplitude uses "shim pulses" to impart an arbitrary spatial phase profile to compensate for the effects of gradients in the static field.[38]

The spin excitation problem is not unlike the case of zero-field NMR,[39,40] where a single axis of quantization is not well defined. Scaling and time-reversal sequences in zero field have been extensively studied[41–45] and represent the three-dimensional generalizations of spin echoes and decoupling sequences. For example, a three-dimensional spin echo can be generated which reverses the sign of I_x, I_y, and I_z

components.[43] Therefore, time-reversal echoes can be generated regardless of which spin operator describes the local quantization axis. For the general case of excitation, matching and shimming in low fields, sequences of noncommuting pulses and gradients could be useful and are being worked on at present as an extension of the present work.

Consider the case of an inhomogeneous static field $\mathbf{B}(\mathbf{r})=B(\mathbf{r})\mathbf{b}(\mathbf{r})$ whose magnitude $B(\mathbf{r})=-\omega_0(\mathbf{r})$ and direction $\mathbf{b}(\mathbf{r})$ varies in space. The axis of quantization of the spin is a function of space: $\mathbf{I}'=\mathbf{I}'(\mathbf{r})$. The Zeeman interaction of a spin in this magnetic field is

$$H=\omega_0(\mathbf{r})T_0^{(1)}[\mathbf{I}'(\mathbf{r})], \tag{27}$$

where $T_0^{(1)}(\mathbf{I}')=I_z'$, $T_{\pm 1}^{(1)}(\mathbf{I}')=\mp(1/\sqrt{2})I_\pm'$ are the rank 1 irreducible tensor operators for spin $\mathbf{I}'$.

If $\mathbf{I}$ is the spin operator in an inertial frame independent of $\mathbf{r}$, this Hamiltonian can be expressed as the Euler rotation

$$H=\omega_0(\mathbf{r})\sum_{m=-1}^{1} D_{0m}^{(1)}[\Omega(\mathbf{r})]T_m^{(1)}(\mathbf{I}), \tag{28}$$

where $\Omega(r)=(\alpha,\beta,0)(\mathbf{r})$ are Euler angles relating the two frames $\mathbf{I},\mathbf{I}'$ at the point $\mathbf{r}$ in space and $D_{0m}^{(1)}[\Omega(\mathbf{r})]$ are elements of the rank 1 Wigner rotation matrix. β is the tilt angle of the axis $\mathbf{I}'$ with respect to $\mathbf{I}$. A transformation to the interaction representation using $U(t)=e^{i\langle\omega_0\rangle t I_z}$, where $\langle B_0\rangle=-\langle\omega_0\rangle$ is the average magnetic-field strength, gives for small values of β

$$\begin{aligned}H=&-\omega_0(\mathbf{r})\frac{\beta}{\sqrt{2}}e^{-i\alpha}T_{-1}^{(1)}(\mathbf{I})e^{-i\langle\omega_0\rangle t}+[(\omega_0(\mathbf{r})-\langle\omega_0\rangle)\\&+\omega_0(\mathbf{r})\beta]T_0^{(1)}(\mathbf{I})+\omega_0(\mathbf{r})\frac{\beta}{\sqrt{2}}e^{i\alpha}T_1^{(1)}(\mathbf{I})e^{i\langle\omega_0\rangle t}.\end{aligned} \tag{29}$$

In high fields, the phase factors $e^{i\langle\omega_0\rangle t}$ average to zero and truncation leaves

$$H=[(\omega_0(\mathbf{r})-\langle\omega_0\rangle)+\omega_0(\mathbf{r})\beta]T_0^{(1)}(\mathbf{I}), \tag{30}$$

the effects of which can easily be refocused using Hahn echoes. Upon going to weaker fields, the phase factors become quasistationary and can be eliminated using rotating-frame versions of the time-reversal sequences of Llor and Pines.[43] This time-reversal averaging is more efficient if the coefficient $\beta\omega_0(\mathbf{r})$ is small. This corresponds to the case of weak curvatures in the magnetic field $\mathbf{B}$. A similar analysis can also be made for rank 2 tensorial interactions.

VI. CONCLUSION

In this paper, I have shown that distortions in the Fourier encoding at ultralow magnetic fields can be substantially reduced by using quadrature rotating-frame gradients. These impart significantly less geometric-phase errors in the encoding. Rather than attempting to eliminate them, the concomitant fields are utilized to provide the required encoding. Calculations show that phase-encoded and slice-selective MRI is possible in ultralow fields using a class of pulses that are combinations of soft and hard pulses to average out undesirable gradient components in low fields.

ACKNOWLEDGMENTS

This work was supported by the Office of Science, Basic Energy Sciences, U.S. Department of Energy under Contract No. DE-AC02-05CH11231. The author would like to thank Alexander Pines for encouraging this work and for stimulating discussions and Josef Granwehr for detailed comments on the manuscript. Useful discussions with Dimitris Sakellariou are acknowledged.

APPENDIX: COMPOSITE SELECTIVE PULSES

Suppose we would like to eliminate the I_y term of the Hamiltonian and use the I_x term for spatial encoding. Two possible approaches can be considered. The first method eliminates I_y by a fast train of 180° pulses applied along I_x. This transforms $I_z \to -I_z$ and $I_y \to -I_y$ and the I_y and I_z terms of the effective Hamiltonian vanish in the limit of short interpulse spacings.

The second method eliminates only the I_y term and is required in the following situation: ac or dc field along I_x, slice-selective gradient field along I_z, and concomitant gradient along I_y. Consider the sequence of four pulses,

$$\{2\tau-(\pi_x)-\tau-(\pi_y)-2\tau-(\pi_{-y})-\tau-(\pi_{-x})-2\tau\}_n. \tag{A1}$$

The refocusing pulses are short, hard pulses, in between which the spins evolve under an arbitrary Hamiltonian of the form $H'(t)=a(t)I_x+b(t)I_y+c(t)I_z$. Over this period of duration 8τ, this pulse sequence produces a time-averaged Hamiltonian $H^{(0)\prime}=\frac{1}{2}(\bar{a}I_x+\bar{c}I_z)$, where $\bar{a}$ is the time average of a. The I_y term is $o(\tau)$ and the scaling factor $1/2$ for I_x and I_z causes a time dilation. Similarly, the following sequence removes the I_z term:

$$\{2\tau-(\pi_y)-\tau-(\pi_z)-2\tau-(\pi_{-z})-\tau-(\pi_{-y})-2\tau\}_n. \tag{A2}$$

It is worth noting that these multipulse sequences are not immune to pulse imperfections. For example, if the π pulses are replaced by $(1-\delta)\pi$ in the above analysis, the pulse error δ appears in first order in the time-averaged Hamiltonian, i.e., $H^{(0)\prime}=\frac{1}{2}(\bar{a}I_x+\bar{c}I_z)+O_1(\delta)I_x+O_2(\delta)I_y+O_3(\delta)I_z$, where $O_i(\delta)\le M|\delta|$ for some $M\in\mathbb{R}$. Compounding these errors over the entire train of pulses typically leads to significant distortions even if the errors are inhomogeneities of a few percent. Therefore, composite pulses or correcting supercycles should be used to relinquish pulse errors to higher order in δ (see, for example, Refs. 46–48).

*URL: http://waugh.cchem.berkeley.edu; Electronic address: lsbouchard@waugh.cchem.berkeley.edu

[1] P. Callaghan, *Principles of Nuclear Magnetic Resonance Microscopy* (Oxford University Press, New York, 1991).
[2] P. Lauterbur, Nature (London) **242**, 190 (1973).
[3] D. Yablonskiy, A. Sustanskii, and J. Ackerman, J. Magn. Reson. **174**, 279 (2005).
[4] M. Mößle, S. Han, W. Myers, S. Lee, N. Kelso, M. Hatridge, A. Pines, and J. Clarke, J. Magn. Reson. **179**, 146 (2006).
[5] S. Lee, M. Mößle, W. Myers, N. Kelso, A. Trabesinger, A. Pines, and J. Clarke, Magn. Reson. Med. **53**, 9 (2004).
[6] R. McDermott, A. Trabesinger, M. Mück, E. Hahn, A. Pines, and J. Clarke, Science **22**, 2247 (2002).
[7] G. Eidmann, R. Savelsberg, P. Blümler, and B. Blümich, J. Magn. Reson., Ser. A **122**, 104 (1996).
[8] B. Blümich, P. Blümler, G. Eidmann, A. Guthausen, R. Haken, U. Schmitz, K. Saito, and G. Zimmer, Magn. Reson. Imaging **16**, 479 (1998).
[9] S. Anferova, V. Anferov, D. Rata, B. Blümich, J. Arnold, C. Clauser, P. Blümler, and H. Raich, Concepts Magn. Reson., Part B **23B**, 26 (2004).
[10] R. Kleinberg, Concepts Magn. Reson. **13**, 396 (2001).
[11] M. Dias, J. Hadgraft, P. Glover, and P. McDonald, J. Phys. D **36**, 364 (2003).
[12] J. Stepisnik, V. Erzen, and M. Kos, Magn. Reson. Med. **15**, 386 (1990).
[13] J. Perlo, V. Demas, F. Casanova, C. Meriles, J. Reimer, A. Pines, and B. Blümich, Science **308**, 1279 (2005).
[14] S. Appelt, F. W. Häsing, H. Kühn, J. Perlo, and B. Blümich, Phys. Rev. Lett. **94**, 197602 (2005).
[15] R. Wang, R. W. Mair, M. S. Rosen, D. G. Cory, and R. L. Walsworth, Phys. Rev. E **70**, 026312 (2004).
[16] W. Shao, G. Wang, R. Fuzesy, E. Hughes, B. Chronik, G. Scott, S. Conolly, and A. Macovski, Appl. Phys. Lett. **80**, 2032 (2002).
[17] M. Augustine, A. Wong-Foy, J. Yarger, M. Tomaselli, A. Pines, D. TonThat, and J. Clarke, Appl. Phys. Lett. **72**, 1908 (1998).
[18] J. Granwehr, E. Harel, S. Han, S. Garcia, A. Pines, P. N. Sen, and Y. Q. Song, Phys. Rev. Lett. **95**, 075503 (2005).
[19] C. Hilty, E. McDonnell, J. Granwehr, K. Pierce, S. Han, and A. Pines, Proc. Natl. Acad. Sci. U.S.A. **102**, 14960 (2005).
[20] C. Meriles, D. Sakellariou, A. Trabesinger, V. Demas, and A. Pines, Proc. Natl. Acad. Sci. U.S.A. **102**, 1840 (2005).
[21] W. Paul, Rev. Mod. Phys. **62**, 531 (1990).
[22] F. Bornemann, *Homogenization in Time of Singularly Perturbed Mechanical Systems*, Lecture Notes in Mathematics (Springer-Verlag, Berlin, 1998).
[23] U. Haeberlen and J. Waugh, Phys. Rev. **175**, 453 (1968).
[24] U. Haeberlen, *High Resolution NMR in Solids, Adv. Mag. Reson. Supplement 1* (Academic Press, New York, 1976).
[25] E. Haacke, R. Brown, M. Thompson, and R. Venkatesan, *Magnetic Resonance Imaging: Physical Principles and Sequence Design* (Wiley, New York, 1999).
[26] R. Turner, Magn. Reson. Imaging **11**, 903 (1993).
[27] M. Berry, *Adiabatic Phase Shifts for Neutrons and Photons*, edited by V. Gorini and A. Frigerio, Vol. 144 of NATO Advanced Studies Institute (Fundamental Aspects of Quantum Theory) (Plenum, New York, 1986).
[28] J. Hannay, J. Phys. A **18**, 221 (1985).
[29] M. Berry and J. Hannay, J. Phys. A **21**, L325 (1988).
[30] D. Chruściński and A. Jamiolkowski, *Geometric Phases in Classical and Quantum Mechanics* (Birkhäuser, Boston, 2004).
[31] N. Higham, SIAM J. Matrix Anal. Appl. **26**, 1179 (2005).
[32] H. Geen, S. Wimperis, and R. Freeman, J. Magn. Reson. (1969-1992) **85**, 620 (1989).
[33] R. Raulet, D. Grandclaude, F. Humbert, and D. Canet, J. Magn. Reson. **124**, 259 (1997).
[34] D. Cory, F. Laukien, and W. Maas, J. Magn. Reson., Ser. A **113**, 274 (1995).
[35] D. Hoult, J. Magn. Reson. (1969-1992) **33**, 183 (1979).
[36] C. Chen and D. Hoult, *Biomedical Magnetic Resonance Technology* (Bristol, New York, 1989).
[37] D. Hoult, G. Kolansky, and D. Kripiakevich, J. Magn. Reson. **171**, 57 (2004).
[38] D. Topgaard, R. Martin, D. Sakellariou, C. Meriles, and A. Pines, Proc. Natl. Acad. Sci. U.S.A. **101**, 17576 (2004).
[39] D. P. Weitekamp, A. Bielecki, D. Zax, K. Zilm, and A. Pines, Phys. Rev. Lett. **50**, 1807 (1983).
[40] D. Zax, A. Bielecki, K. Zilm, A. Pines, and D. Weitekamp, J. Chem. Phys. **83**, 4877 (1985).
[41] A. Llor, Z. Olejniczak, and A. Pines, J. Chem. Phys. **103**, 3966 (1995).
[42] A. Llor, Z. Olejniczak, and A. Pines, J. Chem. Phys. **103**, 3982 (1995).
[43] A. Llor, Z. Olejniczak, J. Sachleben, and A. Pines, Phys. Rev. Lett. **67**, 1989 (1991).
[44] W. Rhim, A. Pines, and J. Waugh, Phys. Rev. B **3**, 684 (1971).
[45] W. Rhim, A. Pines, and J. Waugh, Phys. Rev. Lett. **25**, 218 (1970).
[46] L. Emsley, D. Laws, and A. Pines, in *Lectures on Pulsed NMR, 3rd edition*, Proceedings of the International School of Physics, "Enrico Fermi," Course CXXXIX, edited by B. Maraviglia (Società Italiana du Fisica, Villa Moastero, 1999).
[47] J. Waugh, J. Magn. Reson. (1969-1992) **50**, 30 (1982).
[48] M. Levitt, R. Freeman, and T. Frenkiel, J. Magn. Reson. (1969-1992) **50**, 157 (1982).